2

Water directed phase transformation of mixed surfactant systems

2.1 INTRODUCTION

Surfactants, co-surfactants, water systems self assemble into a broad spectrum of topologically distinct macro-aggregates, among which micellar and lamellar structures have been studied extensively since long [MacKerell, 1995; Tieleman *et al.*, 2000; Marrink *et al.*, 2000; Maibaum *et al.*, 2004; Ma *et al.*, 2009; Bandyopadhyay *et al.*, 1998; Rakitin and Pack, 2004b; Nagle and Tristram-Nagle, 2000; Evans and Wennerstrom, 1994]. Micelles are aggregates in aqueous solution where hydrophilic heads of surfactants are in contact with water and hydrophobic tails form the core in the micelle center. Surfactants self-assemble into micelles at concentrations higher than their critical micellization concentration. The driving force of the formation of these macro-phases is an intricate balance between hydrophobic association at the surfactant-water interface and electrostatic repulsion of head groups each as a function of micelle size [Israelachvili, 1992; Tanford, 1974a,b]. In a lamellar phase, surfactants adopt various interesting topologies to form the ripple $P_{\beta'}$, interdigitated gel phase ($L_{\beta I}$) due to a complex interplay between the surfactant head group interactions and chain packing [Pearce and Scott, 1982a]. Topological features of micelles and lamellae comprising surfactants, polymers, peptides and proteins often mimic biological systems and are used as novel biomedical materials in pharmaceutical sciences, drug delivery and molecular imaging applications [Kim *et al.*, 2009; Nasongkla *et al.*, 2006; Torchilin, 2007; Osada *et al.*, 2009]. A better understanding of factors controlling the phase transformations of these macro-structures can help in developing the technological perspective related to cosmetic formulations, waste water treatment, detergents, secondary and tertiary oil recovery processes and more advanced nano-structure formation concepts [Mørkbak AnneL. *et al.*, 1999; Mulligan *et al.*, 2001; Johannessen and Spildo, 2013; Tadros, 1992; Ramanathan *et al.*, 2013]. Depending on the packing parameter defined by the ratio of the hydrophobic core volume to the area and the critical chain length of surfactants, surfactant-water systems can adopt the most favored structures ranging from micelles, rods, bilayers and vesicles [Israelachvili, 1992; Stephenson *et al.*, 2006; Landazuri *et al.*, 2012; Hayashi and Ikeda, 1980].

Different experimental techniques such as X-ray diffraction, X-ray scattering, electron spin resonance, small-angle X-ray-scattering, electron microscopy, electron paramagnetic resonance, laser light scattering, nuclear magnetic resonance, differential scanning calorimetry and so on are employed to characterize different morphologies and respective physico-chemical properties of self-assembled micelles and bilayers [Müller-Goymann, 2004; Martini and Ciani, 2009; McManus *et al.*, 1993; Basilio *et al.*, 2010; Nagle and Tristram-Nagle, 2000]. Complementary to these experimental studies, computer simulations provide insights into the molecular level interactions responsible for transformations of one macro-structure into another. In recent years computer simulations have opened up a new direction on capturing the self assembly of surfactants into micelles or bilayers using multi-scale simulations. Several coarse grained (CG) models have been developed using all atom (AA) simulations or experimentally known thermodynamics behaviors to derive a complete phase diagram [Shinoda *et al.*, 2008; Posocco *et al.*, 2010; Amani *et al.*, 2011; Thota *et al.*, 2014; Shinoda *et al.*, 2011; Marqusee and Dill, 1986; Verde and Frenkel, 2010]. Although these models can rightly access the relevant time and length scale of micellization or lamellae formation, all atom (AA) molecular dynamics (MD) simulation is particularly useful to probe the atomic level picture. The kinetics of micelle formation via self-assembly is investigated by

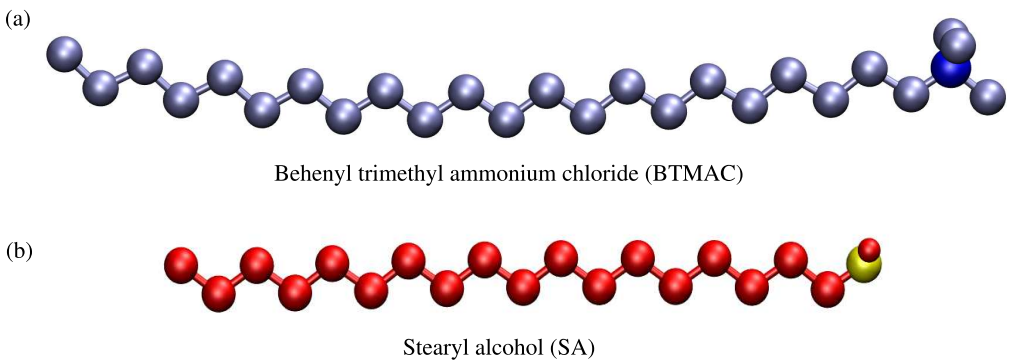

Figure 2.1: Chemical structure of (a) BTMAC and (b) SA molecules in atomistic representation. Color codes: Blue, BTMAC head (N+); Ice-blue, BTMAC chains; Red, SA chains; Yellow, SA head (O); White, Hydrogen.

AA simulations although formation of finite size large aggregates is associated with it [Sammalkorpi *et al.*, 2007]. The self assembly of Triton-X micelles are studied at different concentrations and temperatures [Yordanova *et al.*, 2015]. The effects of molecular parameters like the size, the chain length and the form of the head-group on cationic and anionic micelles are investigated [Aoun *et al.*, 2015]. Similarly, an asymmetric sawtooth 1D ripple phase consisting alternate non-interdigitated gel-like domain, and a fully interdigitated ($L_{\beta I}$) domain, is reported [Anzo *et al.*, 2003; de Vries *et al.*, 2005] for the dipalmitoylphosphatidylcholine (DPPC) lipid bilayer using a united atom model (UA), where the formation of ripple phase is dependent on temperature and hydration. However, none of these studies shed light on how one micellar phase can be transformed to a lamellar phase by controlling a parameter such as hydration.

In this chapter, different phases of surfactant and co-surfactant aggregates are reported, which are studied using AA simulations. In comparison to the well studied lipid bilayers, mixed surfactant micelles have recieved received lesser attention. Here we report simulations for aggregates composed of the cationic surfactants, behenyl trimethyl ammonium chloride (BTMAC) along with co-surfactant, stearyl alcohol (SA) and show that varying the water concentrations offers a flexible way to control the macro-structure. The MD simulations of the mixed surfactant aggregates reveal the presence of few micellar aggregates at a given water content. With decreasing water concentration at a fixed BTMAC to SA ratio, the micellar phase can be transformed to a one dimensional interdigitated ripple phase which disappears at higher temperature. The atomistic molecular dynamics simulations indicate that decreasing the water concentration induces specific head-group area which is coupled with the critical chain length or thickness to obtain a packing parameter associated with a given phase. The study opens up a compositional route which can be utilized in controlling and designing phases with desired structure based functionalities.

2.2 COMPUTATIONAL DETAILS

Atomistic simulations are carried out for a mixed surfactant system composed of cationic surfactant BTMAC (formula: $CH_3-(CH_2)_{21}-N^+Cl^--(CH_3)_3$) and co-surfactant SA (formula: $CH_3-(CH_2)_{17}-OH$) at a ratio of 2:1. All the simulations are performed using GROMACSv4.6.5 [Abraham *et al.*, 2018; Bekker *et al.*, 1993; Berendsen *et al.*, 1995; Lindahl *et al.*, 2001; van der Spoel *et al.*, 2005; Hess *et al.*, 2008; Pronk *et al.*, 2013; Páll *et al.*, 2015; Abraham *et al.*, 2015] and VMDv1.9 [William *et al.*, 1996] is used for visualizing the structures and generating the snapshots. The snapshots of chemical structures of BTMAC and SA are shown in figure 2.1 (a) and (b). The atomistic force-fields of BTMAC and SA are obtained from Gromos-87 van Gunsteren and

Berendsen [1987] and OPLS-AA Jorgensen [1986]; Kaminski *et al.* [2001] and partial charges used for BTMAC and SA are reported in table Using the all atom force-field of BTMAC and SA, the gel

Table 2.1: Masses and charges of atoms of BTMAC and SA used in the atomistic simulations. These parameters are taken from the previously studied system [Debnath *et al.*, 2009].

BTMAC			SA		
Atom	Mass	Charge	Atom	Mass	Charge
CP_2	14.027	0.0	CP_2	14.027	0.0
CP_3	15.035	0.0	CP_3	15.035	0.0
CH_2	14.027	0.3	CH_2	14.027	0.265
LNL	14.0067	-0.5	O	15.9994	-0.7
$(LC_3)_3$	15.035	0.4	H	1.008	0.435

to liquid crystalline phase transition temperature obtained from experiment is correctly reproduced and reported earlier [Debnath *et al.*, 2009]. The simulations are carried out by varying water content ranging from 84.56 wt.% to 62.35 wt.%. For each of the simulations, 100 BTMAC molecules and 50 SA molecules are placed randomly in a box followed by solvation with water using the SPC water model [Mark and Nilsson, 2001]. The number of water molecules to get the desirable water concentration is shown in table 2.2. To neutralize the positive charges due to BTMAC, 100 chloride ions are added in the system. All the six systems are energy minimized using the steepest descent algorithm [Leach, 2001]. This is followed by simulation in an NVT ensemble for 100 ps at 283 K. Once the systems reach thermal equilibrium, 20 ns NPT simulations are performed. To maintain the constant temperature, Berendsen thermostat [Berendsen *et al.*, 1984] is with coupling constants are 0.5, 1 ps. The pressure is held constant at 1 bar using Berendsen semi-isotropic coupling [Berendsen *et al.*, 1984] and the trajectories are collected at every 100 ps. The integration time-step is 2 fs in all the simulations. Coulombic interactions are treated with Ewald method [Ewald, 1921] and a cut-off of 1.3 nm is used to compute the van der Waals interactions. It is found that the several simulations carried out with variable water concentrations result in either co-existence of two phases or are in the similar phase. Hence all further simulations and analyses are carried out for the systems with the two extreme water concentrations.

To overcome the system size effect, larger systems A1 and A2 are prepared which have water concentrations similar to S1 and S2 respectively. Both these systems are simulated in an NPT ensemble for 300 ns with the same set of simulations parameters used earlier. The equilibration of the simulations is monitored by computing the solvent accessible surface area (SASA) for BTMAC and SA. Last 120 ns are analyzed for the analyzing the properties of these systems. Simulations are also performed for different box dimensions for both A1 and A2 systems to investigate the system size effect and are referred to as BA11, BA21 and BA22. The details of all the systems

Table 2.2: Number of molecules of BTMAC, SA and water used in different water concentrations investigated. BTMAC to SA ratio is fixed at 2 : 1. The percentage of water decreases from S1 to S2.

System	BTMAC molecules	SA molecules	Water molecules	NPT (ns)	Wt% of water
$S1$	100	50	16373	20	84.56
S_a	100	50	9961	20	76.90
S_b	100	50	6310	20	67.83
S_c	100	50	6150	20	67.28
S_d	100	50	5970	20	66.72
S_e	100	50	5290	20	63.80
$S2$	100	50	5950	20	62.35

and their respective simulation run lengths are reported in table 2.3. It is seen that at 84.56 wt.% and 62.35 wt.% water concentration, the surfactants self-assemble to form spherical micelles and lamellar phase respectively. All the analyses to understand the structural properties of the systems investigated are discussed in the next section.

Table 2.3: Number of molecules of BTMAC, SA and water in different systems investigated. BTMAC to SA ratio is fixed at 2 : 1 in A1 and A2. The percentage of water decreases from A1 to A2.

System	Number of molecules			Water %	Box-length (nm)			NPT (ns)
	BTMAC	SA	Water		L_x	L_y	L_z	
A1	400	200	65492	84.56	11.45	11.45	18.08	300
A2	400	200	19800	62.35	17.26	17.26	3.26	300
BA11	400	200	65492	84.56	17.47	17.47	7.78	170
BA21	800	400	39600	62.35	17.26	17.26	6.51	200
BA22	1600	800	79200	62.35	17.26	17.26	13.02	80

To examine the effect of temperature on the spherical micellar and lamellar phases, the simulations are carried out in the temperature range of 283-345 K. The initial configuration of the systems at 300 K is obtained from the final configurations of small systems S1 and S2 with an annealing rate of 29.4 ps/K. The systems are equilibrated in an NVT ensemble for 100 ps which is followed by 25-45 ns simulation in NPT ensemble. Similar protocol is followed to obtain the initial configurations at other higher temperatures (323 K, 330 K, 338 K and 345 K). The final configurations at the lower temperature is used to generate the initial configuration at the next higher temperature using the same annealing rate followed by NVT and NPT runs. Once the systems S1 and S2 at all the temperatures reach equilibrium, larger systems are generated from these configurations with system sizes similar to A1 and A2. All the larger systems at higher temperatures are simulated for 100 ns in NPT ensemble. The simulation parameters are same as for A1 and A2 at 283 K.

The role of temperature on bilayer thickness and interdigitation at different temperatures is understood by plotting Voronoi diagrams in MATLAB. Both the bilayer thickness and interdigitation are superimposed on the Voronoi head group areas. The head-group density profiles of BTMAC and SA are used as the geometric criteria to differentiate between the surfactants belonging to upper (L_u) or lower (L_l) monolayer. The Voronoi cell areas are calculated using MATLAB and represent the area occupied by both BTMAC and SA headgroups. Delaunay triangulation is carried out L_u and L_l using the head-group co-ordinates. The surfaces $z_u(x, y)$ and $z_l(x, y)$ are obtained by interpolating the triangulated surface on the grids of dimensions $n_x \times n_y$. The thickness of the bilayer, $d(x, y)$, is the thickness computed from the head to head distances between two layers. It is computed as,

$$d(x, y) = z_u(x, y) - z_l(x, y) \tag{2.1}$$

where $z_u(x, y)$ and $z_l(x, y)$ are the co-ordinates of the heads of two leaflets, $l1$ and $l2$ respectively along the bilayer normal direction. Similarly, the interdigitation, $I(x, y)$, within the surfactant chains across the layer is calculated by computing the difference in the z-co-ordinates of the end beads between the two leaflets as a function of the bilayer surface. Mathematically it is represented as,

$$I(x, y) = z_{u,end}(x, y) - z_{l,end}(x, y) \tag{2.2}$$

where $z_{u,end}(x, y)$ and $z_{l,end}(x, y)$ are the coordinates of the end beads of less and more populated leaflets respectively along the bilayer normal direction.

2.3 RESULTS AND DISCUSSIONS

Effect of water concentration

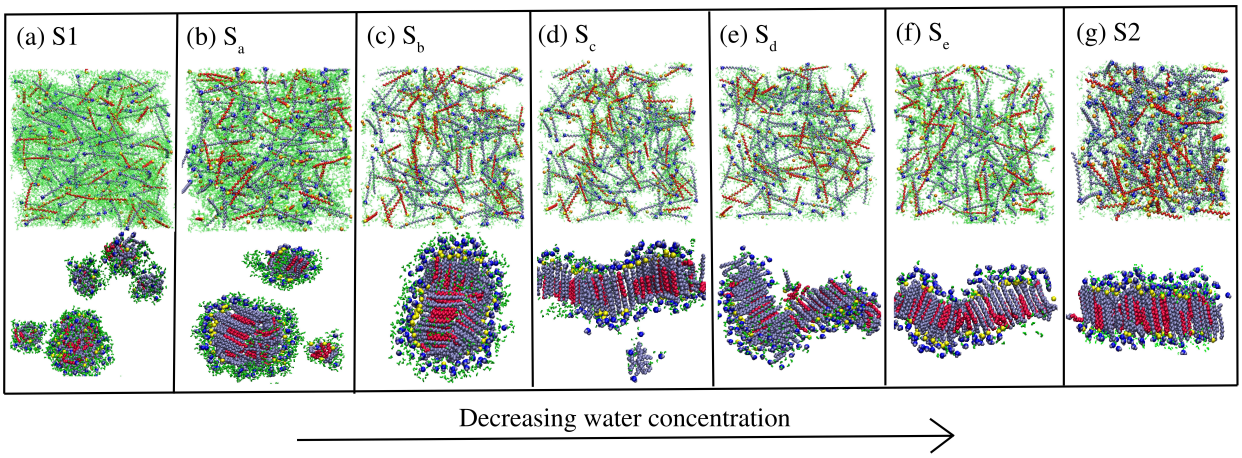

Figure 2.2: Snapshots of systems S1 to S2 (reported in table 2.2) with decreasing water concentration and the BTMAC to SA ratio at 2:1. (a)-(g) show the random initial configurations and the final configurations after self-assembly of the all systems obtained after 20 ns. Color codes: Blue, BTMAC head (N+); Ice-blue, BTMAC chains; Red, SA chains; Yellow, SA head (O); White, Hydrogen; Orange, (Cl^{-1}) and green, water. In the final configurations, all of the water molecules are not shown for the sake of clarity. Micelles are transformed into bilayers where the shape slowly changes from sphere to ellipse to bilayers. The water concentrations below which it is a bilayer is 67.28 wt %.

As described in the table 2.2, the snapshots of all the systems from S1 to S2 after self-assembly is shown in figure 2.2. It is seen that starting from random initial configurations, all the systems self-assemble to form aggregates of either micellar shape or bilayer. The snapshots of the systems show that at a higher water of 84.56 wt% (S1), the surfactants self-assemble to form spherical micellar aggregates which are also present at the next lower water concentration i.e., 76.9 wt% (S_a). However, at further decrease in water concentration although the micellar shape of the surfactant assembly is preserved, but the spherical micelles fuse to form a single aggregate in cylindrical shape at 67.83 wt% (S_b). As the water concentration is decreased slightly from 67.83% to 67.28% (S_b to S_c) , a phenomenal change in aggregation behavior is seen. The snapshot of self-assembled surfactants shows the co-existence of both the lamellar aggregate and a micellar aggregate. At a further decrease in water concentration from 66.72 wt% to 62.35 wt% (S_d to S2 in table 2.2), the micellar phase vanishes and only the lamellar phase is found to exist. Hence the the critical water concentration below which a bilayer is formed is ∼67.28 wt%. The water directed phase diagram of surfactants shows that keeping a fixed BTMAC and SA ratio (2:1), a decrease the water concentration leads to a phase change from micelles to bilayer. Since self-assembly of systems S_a to S_e result into similar phases as found in S1 and S2, (systems with extreme water concentrations) or show the co-existence of phases, all analyses discussed in the further sections are only for the systems with two extreme water concentrations.

Shape and size of aggregates

Figure 2.3 shows the final configurations of A1 and A2 systems have larger system size with the water concentrations same as in S1 and S2. From the snapshots, it is found that at a higher water content, system A1 shows the presence of few spherical micelles. On the other hand, system A2 having low water content, shows the existence of a double bilayer. The equilibration of

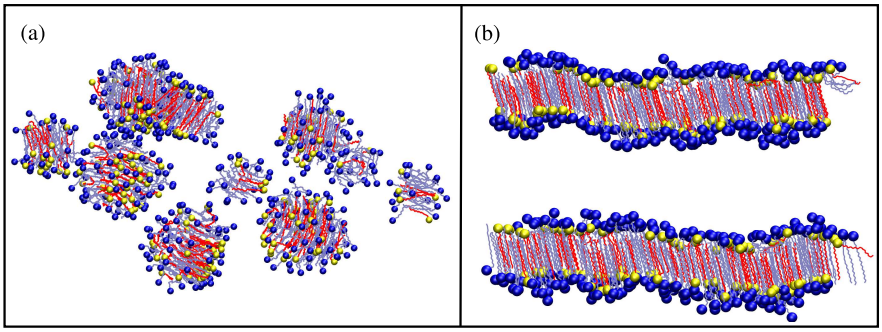

Figure 2.3: Snapshot of (a) A1 with 84.56 wt% of water and (b) A2 with 62.35 wt% water. The color code is same as used in figure 2.2 Water molecules and chloride ions are omitted for the sake of clarity.

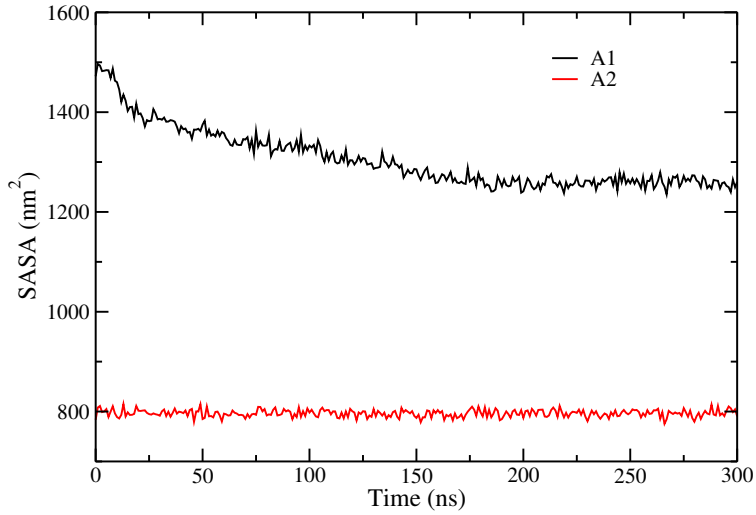

Figure 2.4: Time evolution of solvent accessible surface area (SASA) for A1 and A2. The SASA is converged for the last 120 ns for both A1 and A2.

these self-assemblies is monitored by the convergence of time evolution of SASA of the surfactants. From the SASA plot, shown in figure 2.4, it is found that after 180 ns of the simulation the SASA converges well for both the systems. Hence the trajectory after 180 ns, i.e. the last 120 ns is considered for the production run. The shape and size of A1 is determined by analyzing the radial distribution function (RDF, $g(r)$). The $g(r)$ is calculated for BTMAC and SA heads from the center of mass (COM) of last tail beads for all the micelles. The distance from the COM of end tail beads to the head groups determines the size of micelle. A bin-width of 0.02 nm is chosen to compute $g(r)$. The radial distribution function is calculated using the following formula

$$g(r) =< \frac{1}{\rho_N} \sum_{i=1}^{N} \sum_{j=1}^{N} \delta(r_{ij} - r) > \tag{2.3}$$

where r_{ij} denote the distances between the two particles i, j and N signifies the total number of particles. ρ denotes mean particle density and the angular brackets show the averaging over time. The micelles having similar size distribution are averaged and are classified as one class of micelles. Figure 2.5 shows the micellar size distribution, averaged over similar class of micelles. $M1$, $M2$

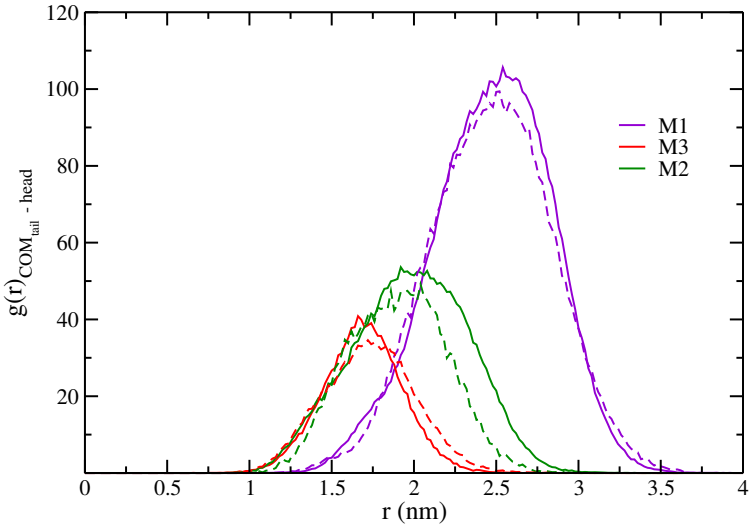

Figure 2.5: g(r) of head of BTMAC and SA from the center of mass of the last bead of the tails for M1, M2, M3 are shown for A1 and BA11. The distribution function from simulations with larger system-size match well.

and $M3$ represent the three distinct classes of micelles which differ in terms of their sizes. The x-axis of the plot denotes the distance of the head group from the COM of the end tail bead. The $g(r)_{COM_{tail}-head}$ is symmetric in shape with respect to the peak locations for all class of molecules. This quantifies the spherical nature of the micellar aggregates which is also evident from the snapshots shown in figure 2.3. The location corresponding to the maximum peak height can be considered as the radii of the micelles. This shows that the micelles belonging to class M3 are smallest in size. Micelles of class M2 have greater sizes than M3 and again M1 has greater size than M2. Similar analysis is performed for the system larger system BA11, mentioned in table 2.3. The radial distribution function determining the micellar size in system BA11 reveal the existence of micelles with similar radii as in A1. Three classes of micelles are formed and the comparison of A1 with BA11 is shown in figure 2.5. This demonstrates that although the system sizes of these two systems are different, the $g(r)_{COM_{tail-head}}$ match reasonably well. Similarly, the structure of system A2 having lower water content is analyzed by computing the density profiles of BTMAC and SA with respect to the bilayer normal. A bin width of 0.01 nm is chosen for the calculation of density. Figure 2.6 shows the density distribution of the surfactants. It is seen that there are two aggregates having similar densities, named as B1 and B2 respectively. This refers to an equal number of surfactants in each of the aggregate which is consistent with the snapshot shown in figure 2.3(b). The density of the two separate layers in each of the aggregates are found to overlap where the lower layer has higher density than the upper layer. The overlapping densities of the two leaflets in an evidence of strong interdigitation in the surfactant chains. The head group densities show unequal peak heights where the lower layer has higher head group density. This illustrates that there is a compositional asymmetry in the two bilayers. Similar results are found for the bilayers BA21 and BA22 which have larger system sizes but the water content similar to A2. It is identified that the density distributions of BTMAC and SA are not affected by the system sizes and also, the compositional asymmetries and interdigitations remain unchanged.

To learn the configuration of surfactant chains in A1 and A2, the angle distribution of both BTMAC and SA chains are calculated. Two vectors, defined from the tail-to-middle and middle-to-head, are taken into consideration. The angular distribution between these two vectors is computed which is averaged over all the surfactants in A1 and A2 and is shown in figure 2.7. This analysis is useful to illustrate if the surfactant chains are stretched or folded inside the micellar or the lamellar aggregate. The average angles of BTMAC and SA are $\sim$141.236° and $\sim$159.769°

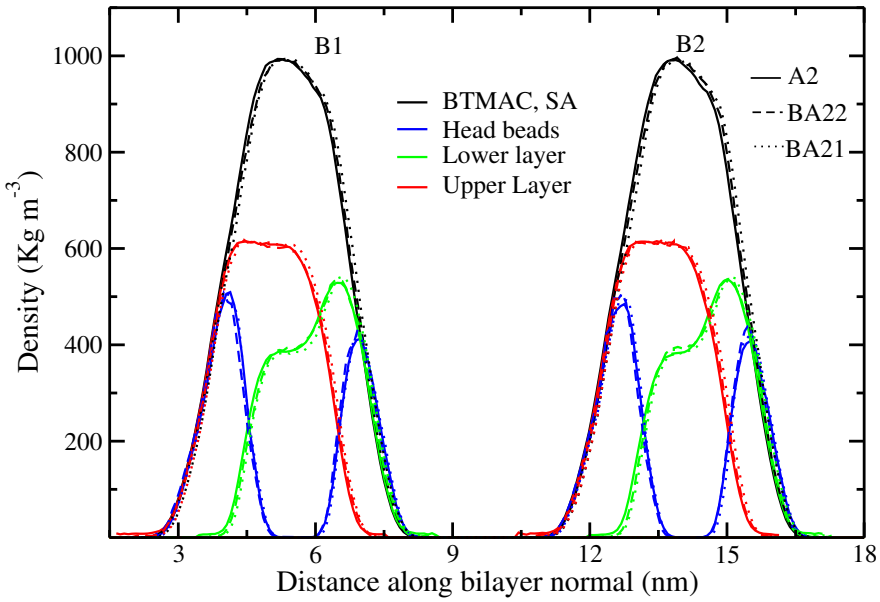

Figure 2.6: Density profiles of systems A2, BA21 and BA22 which have lower water content. These systems are simulated with different box-lengths to check the system size effect.

respectively in A1. On the other hand, the average angle for head-middle-end angle distribution of

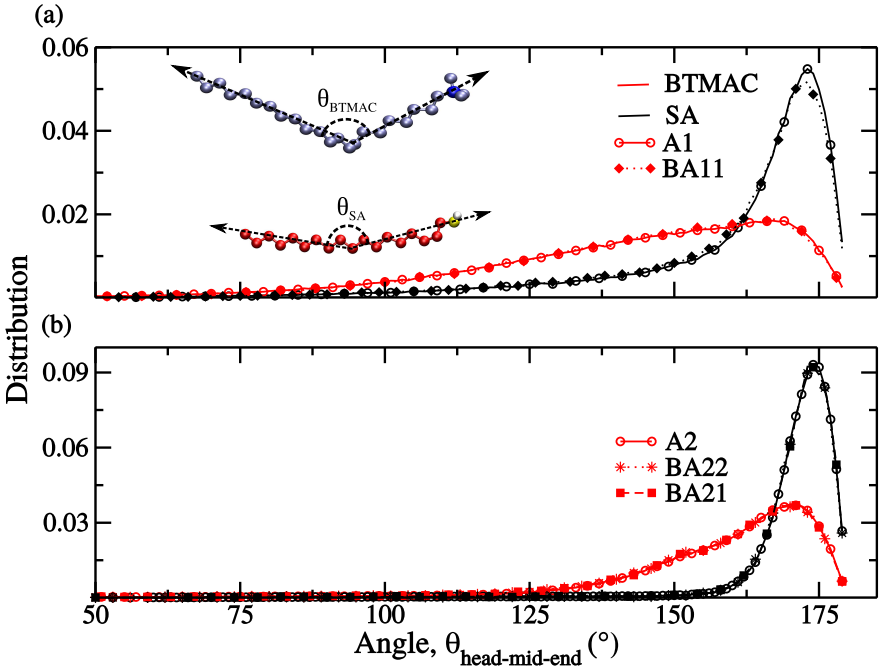

Figure 2.7: Angle distribution of head-middle-end of BTMAC and SA chains for (a) systems A1 and BA11 which have higher water content (84.56 wt%), (b) systems A2, BA21 and BA22 having lower water content (62.35 wt%). The schematic representation of vectors considered to compute the angular distribution are shown in the inset of subfigure (a) where θ signifies the angle between the two vectors.

BTMAC and SA in A2 are ∼169.689° and ∼156.467° respectively. The locations of most probable peaks in A1 and A2 reveal that the surfactant chains are straight. However, the distributions of BTMAC and SA are narrower in A2 than in A1. This can be attributed to the occurrence of

micelles of different sizes which causes a wide angular distribution. On the other side, due to the lamellar phase in A2, the surfactant chains extend in the direction of opposite leaflets and remain stretched due to interdigitation. The distributions in respective larger systems are also in good agreement with the distributions of A1 and A2. Hence it is clear from the figure that the chains of both BTMAC and SA are fully stretched and not folded back.

The close-packing or the compactness in A1 is monitored by measuring the radius of gyration (R_g), using the following equation,

$$R_g = \sqrt{\frac{\sum m_i r_i^2}{\sum m_i}} \tag{2.4}$$

where m_i is the mass of any atom i at a distance r_i from the COM of the aggregate core. Thus, R_g is a measurement of the mass distribution of the surfactants which constitute the aggregate with respect to its COM. Thus R_g is an estimation of the size of the micellar aggregate. The R_g for the three classes of micelles $M1$, $M2$ and $M3$ are obtained after averaging over all the surfactants present in the respective class of micelles for the production run (last 120 ns). Figures 2.8(a), (b) and (c) show the R_g for $M1$, $M2$ and $M3$ respectively. The R_g for each class of micelle is also calculated from the hydrodynamic radius, R_h which is obtained from the respective $g(r)$. The mathematical relationship between R_g and R_h is given as,

$$R_g = \sqrt{\frac{3}{5}} R_h \tag{2.5}$$

The radius of gyration computed from equations 2.4 and 2.5 are plotted and the comparisons of R_g obtained from these two relations is shown in figure 2.8. The magnitude of error bars from equation 2.4 are comparable to the size of symbols for individual M1, M2 and M3 and are hence not shown in the figure. The average R_g values obtained from $g(r)$ for the three classes of micelles shown in figure 2.5 are found to be $\sim$ 1.16 nm, $\sim$ 1.55 nm and $\sim$ 1.94 nm respectively. The error bars in the values of R_g are also shown for each class of micelle. From figure 2.8, it is clear that these values are consistent with the R_g obtained from equation 2.4. We also compute the R_g averaged over all class of aggregates in system A1 which turns out to be 1.62$\pm$0.29 nm and is shown in figure 2.8(d). The figure shows large error bars which are attributed to the differences in the sizes of $M1$, $M2$ and $M3$. The values of R_g do not change with the evolution of time. This denotes that the micelles do not change their shapes and maintain their compactness during the simulation which depicts the stability of the self-assembled aggregates. Subfigure 2.8(e) represents the eccentricity of both the systems A1 and A2. Mathematically the eccentricity (e) is given as,

$$e = 1 - \frac{I_{min}}{I_{avg}} \tag{2.6}$$

where I_{min} is the minimum of moment of inertia and along the x, y and z and I_{avg} is the average of moment of inertia along the three axes. Eccentricity gives the measurement of any deviation from the spherical shape. For any perfect sphere, the value of e is zero. Hence any deviation in the spherical shape in A1 and A2 can be determined from the values of e. From the figure, it is clear that the eccentricity for system A1 is close to zero. The average e for A1 is 0.11$\pm$0.04 which dictates the spherical nature of the micelles in A1. Contrarily, since A2 self-assembles to form bilayers, it is recognized from the figure that e for A2 is comparatively much higher than A1 with an average value of 0.60$\pm$0.01. The time variations in e for both A1 and A2 do not change which attribute to the stability of their respective shapes.

Molecular shape in aggregates

The arrangement of surfactant chains in the two leaflets strongly affects the architecture and phase of the aggregates. For understanding the shape and orientations of the surfactant molecules

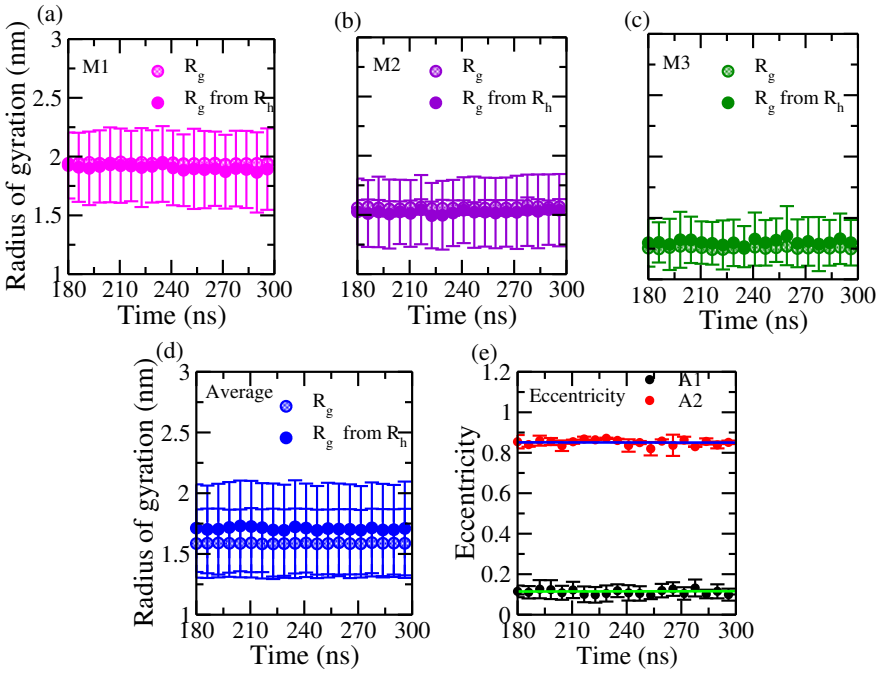

Figure 2.8: Time evolution of radius of gyration (R_g) of (a) M1, (b) M2, (c) M3, (d) average for system A1 after averaging over all aggregates. Error bars of R_g calculated from equation 2.4 are not shown for individual M1, M2 and M3 since their sizes are of the sizes of the symbols. Error bars of R_g calculated from R_h are shown.

constituting the aggregates, the deuterium order parameter (S_{CD}) is calculated for both BTMAC and SA. Since a united atom model is used for the current study, the location of H-atom (or deuterium, D) is predicted on the basis of the tetrahedral structure of the methylene group of C_i, for which S_{CD} has to be evaluated. A z-axis is chosen by joining C_{i+1} to C_{i-1}. x and y axes are chosen perpendicular to the z axis and S_{xx} and S_{yy} are evaluated following the equation,

$$S_{xx} = S_{yy} = \frac{1}{2}(< 3cos^2\beta - 1 >). \tag{2.7}$$

Here β is the angle between the CD bond vector and the bilayer normal. Finally S_{CD} is calculated as follows [Douliez *et al.*, 1998],

$$S_{CD} = \frac{2}{3}S_{xx} + \frac{1}{3}S_{yy} \tag{2.8}$$

The value of S_{CD} explains the alignment of chains with respect to the bilayer normal. If S_{CD} is 1, it shows a perfect alignment with the bilayer normal, -0.5 means anti-alignment and 0 describes that the molecule is randomly oriented with respect to the normal axis. The order parameter is computed for every C-atom along the chains of BTMAC and SA and is averaged over all the molecules. The order parameter is plotted for systems with high and low water contents and is shown in figure 2.9(a) and (b). For both the surfactant molecules, S_{CD} is close to zero in systems with higher water content (A1 and BA11). This is attributed to the isotropic orientational order of the spherical micellar aggregates. The S_{CD} for other systems with low water content (A2, BA21 and BA22) is higher than the order of micellar aggregates because of fully stretched order of BTMAC and SA along the bilayer normal. From the analysis, it is also evident that the systems with similar water content show similar order parameter.

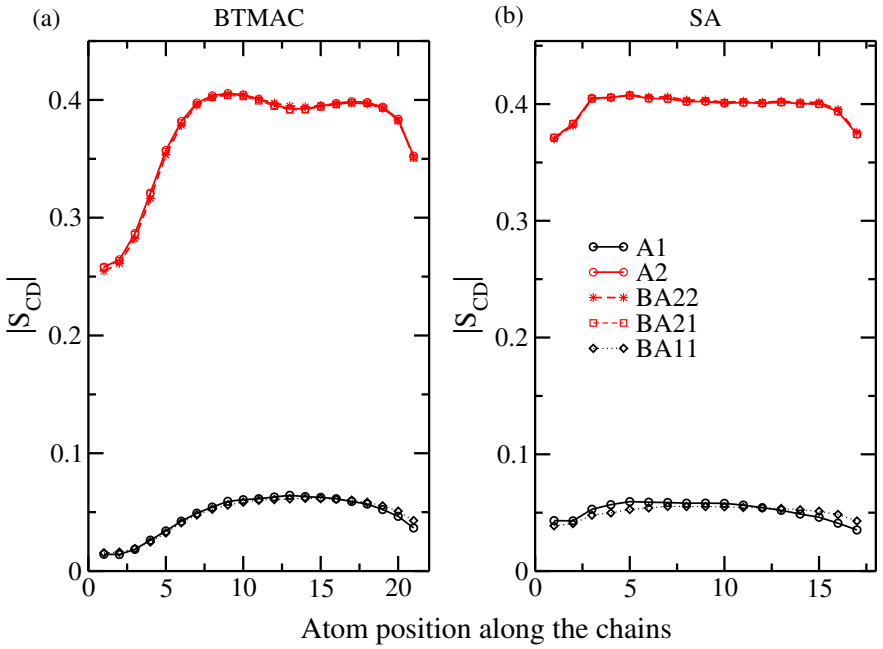

Figure 2.9: Deuterium order parameter (S_{CD}) of (a) BTMAC (b) SA after averaging over all aggregates. S_{CD} of systems A1 and BA11 having higher water content is close to zero for both BTMAC and SA due to the spherical nature of the micelles.

Effect of temperature

The effect of temperature in A1 and A2 are investigated by carrying out simulations at higher temperatures (300 K, 323 K, 330 K and 345 K) as mentioned in the simulation details. The aggregation number in A1 shows remarkable changes upon heating from 283 K to 330 K. Although, at 330 K the phase of the system remains unchanged. The aggregation number in A1 at the temperatures 283 K, 300 K, 323 K and 330 K are shown in figure 2.10. Once the temperature is raised from 283 K to 300 K, the 10 micellar aggregates fuse to form 8 aggregates. A further rise in temperature to 323 K results into the fragmentation of micelles leading to the formation of 11 aggregates. Again upon rising the temperature to 330 K there are 8 aggregates (figure 2.10(d)) which remain stable upto 345 K (data not shown). The heights of bar plot increase for few aggregates of $M1$ and $M2$ classes from 283 K to 300 K and micelles of class $M3$ disappear. This indicates that the micelles of classes $M1$ and $M3$ accommodate the surfactants of class $M3$ resulting into the fusion of micelles. The $M3$ class of micelles reappear at 323 K and the bar height of some of the aggregates of $M1$, $M2$ again decrease, signifying the fragmentation of surfactants from large size aggregates to produce micelles of smaller sizes. This indicates that the appearance or the disappearance of class $M3$ is dependent upon the fusion and fragmentation mechanisms of classes $M1$ and $M2$. This phenomena is again evident from the fusion mechanism at 330 K. As the amount of water decreases from A1 to A2, the micellar phase transforms into a lamellar phase at 283 K. The density profile diagrams of the two leaflets confirms the presence of interdigitation in the bilayer. To further investigate the phase of the bilayer at higher temperatures, the bilayer thickness and interdigitation of A2 is computed at 283 K, 338 K and 345 K. The bilayer thickness is computed using equation 2.1 and is superimposed on Voronoi area per head groups. Figure 2.11(a-c) show the variations of bilayer thickness upon increasing temperatures from 283 K to 338 K to 345 K. From figure 2.11(a), it is clearly visible that there exists a periodic modulation in the bilayer thickness which characterizes a ripple phase bilayer. Upon heating to 338 K, the extent of modulation in bilayer thickness decreases although the ripple phase remains stable at this temperature. The variation in bilayer thickness at 338 K is visible from figure 2.11(b). Once the temperature is raised to 345 K,

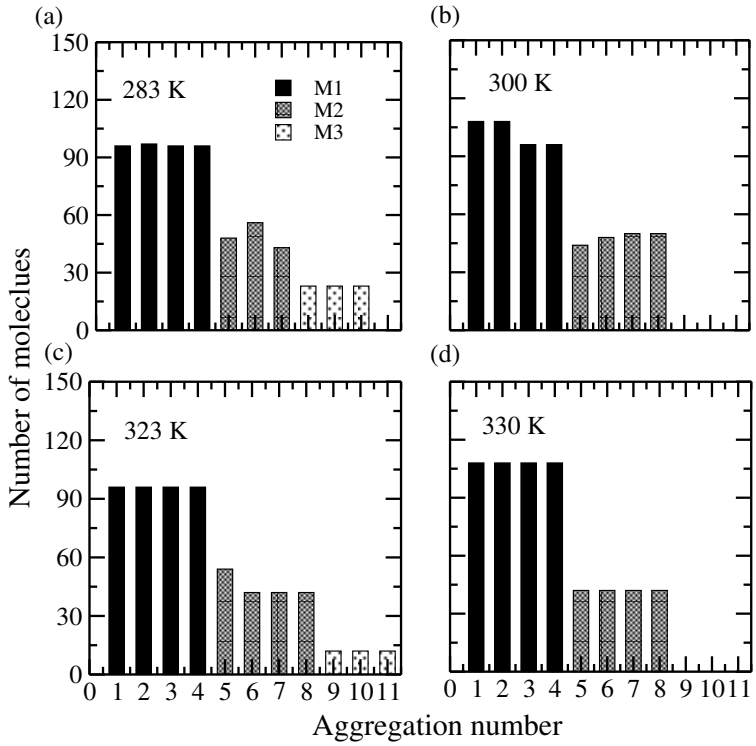

Figure 2.10: Number of aggregations present in A1 at (a) 283 K, (b) 300 K, (c) 323 K and (d) 330 K. Different aggregates get fused together or fragmented with different temperatures.

periodic variation in bilayer thickness vanishes. This indicates that the ripple phase of the bilayer is not preserved at 345 K. The interdigitation in the bilayers is computed using equation 2.2 and is plotted on the Voronoi area per head groups in figures 2.11(d-f). Interdigitation in the bilayers is quantified from the negative numbers shown in the colorbar, similar as followed in [Khakbaz and Klauda, 2018]. From the figures, it is seen that the bilayers are interdigitated, although there is variation in the level of interdigitation along the surface. This identifies a ripple phase bilayer at temperatures 283 K and 338 K which disappears at 345 K. A comparison of bilayer thickness and interdigitation at the respective temperatures of 283 K and 338 K reveal that in the depleted regions with less thickness, the chains show strong interdigitation. However, due to ripple phase, some of the regions in the bilayers have higher thickness due to which the interdigitation in the chains is reduced. At 345 K, the ripple phase of the bilayer departs but the inverse relationship in bilayer thickness and interdigitation of the surfactant chains holds good. Nevertheless, the area per head group shows no significant increase upon increasing the temperature. This signifies that the bilayer does not melt at 345 K, but the one dimensional ripple phase transforms into an interdigitated gel phase ($L_{\beta I}$).

Influence of water content on geometric packing

It is well known that the surfactant molecules self-assemble into different shapes leading to a wide variety of macro-aggregates. The self-assembly of surfactants is driven by different conditions such as pH, temperature or ionic strength. A change in these conditions could lead to the transformation of a well defined aggregate into another which is induced by two opposing interactions: hydrophobic association and the head-head repulsion which acts at the hydrocarbon-water interface. These two competing forces of interactions lead to the formation of an optimal head-group area for surfactant molecules, where the head group is exposed towards the water interface. This acts as the driving framework for the geometric packing of molecules to form

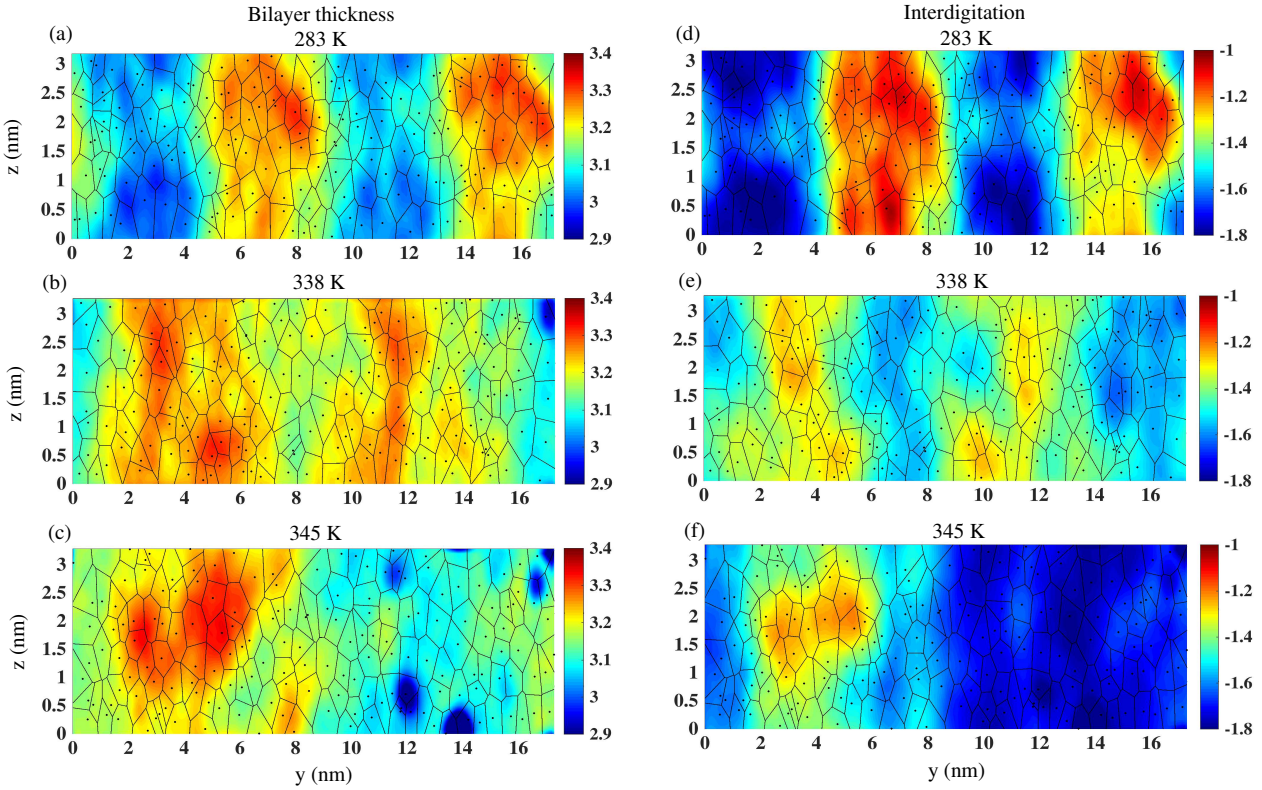

Figure 2.11: Bilayer thickness (a-c) and interdigitation (d-f) superimposed on Voronoi area per head group at 283 K, 338 K and 345 K. The unit of all color bars is in nm. The plot shows the presence of rippling along y-axis till 338 K which disappears at 345 K.

aggregates. In the present work, the water content shows a major role in establishing the optimal head-group area per surfactant which is required for a specific macro-aggregate.

At a fixed BTMAC to SA ratio and higher water content, the surfactants self-assemble and lead to the formation of spherical micelles in A1. These micelles are categorized into three sub-classes $M1$, $M2$ and $M3$ which differ in the terms of the radii of micelles. Upon decreasing the water content, the micellar phase transforms into a lamellar phase in system A2. The $g(r)$ of the surfactant heads with respect to the COM of the last tail beads approves the spherical symmetry as well as the radii of three classes of micelles. The approximate radii (R) of the spherical micelles is determined from the location of the $g(r)$ peak. The area per head gr up (a_0) of BTMAC and SA is calculated using the equation $a_0{=}4\pi R^2/M$, where M is the aggregation number of each spherical micelle. The average value of a_0 after averaging over all the three classes of micelles is found to be 1.16±0.31 nm^2 for system A1. Similarly, the approximate critical chain length (l_c) is determined from the average location of peaks obtained from the head-to-tail distributions. The l_c for surfactant chains in A1 is found to be 2.62±0.12 nm. In system A2, which has lower water content, the a_0 is determined from the surface area of the box which is divided by the number of surfactant molecules in one leaflet. The average a_0 (0.38±0.06 nm^2) in system A2 which is obtained by averaging over 4 surfaces from two bilayers. The a_0 value decreases from A1 to A2 because of less availability of the water molecules which surround the head groups. The reduction in a_0 due to the less hydrated surfactant head-groups is coupled with an increment in the critical chain length. The l_c for system A2 is determined from the bilayer thickness which is found to be 3.14±0.09 nm. Comparing the systems with higher water content to those with the lower water content, it is seen that the a_0 decreases and l_c increases upon lowering the amount of water. An interplay between the coupled area per head-group (a_0), critical chain length (l_c) and the volume of the hydrophobic core can be accountable for the essential packing parameter which is associated with the phase transformation

from spherical micellar to lamellar phase. Hence, a lowering in a_0 due to the less availability of water molecules around the surfactant heads lead to a phase transformation in macro-structure from spherical micelles to bilayers.

2.4 SUMMARY AND CONCLUSIONS

In this chapter, the all-atom molecular dynamics simulations are carried out to investigate the influence of water concentration upon the phase transformation of a model surfactant/co-surfactant/water system. At a high water concentration of 84.56 wt%, the surfactants form spherical micelles via self-assembly. Upon decreasing the water concentrations from 84.56 wt% to 62.35 wt%, the spherical micellar phase changes to a lamellar phase. The critical water concentration below which a bilayer is formed is found to be ∼67.28 wt%. All the structural properties are found to remain unaffected by changing the system sizes. The $g(r)$ of head-groups with respect to the COM of the end tail bead is calculated. The peak location determines the approximate radii of the micelles. On the basis of micellar size distributions, it becomes clear that the micelles fall into three distinct classes. At the lower water concentration, the density profile of the surfactants in the two leaflets shows an overlap which ensures the presence of interdigitation in the bilayer. Dissimilar heights of head-group density indicate towards the existence of asymmetric bilayers obtained from self-assembly. The head-middle-end angle distribution for systems with high water content shows a broad distribution due to the formation of micelles of different sizes. The time evolution of radius of gyration and eccentricity remains unchanged during the production run. This corroborates the stability of the structures. The order-parameter is lower at high water content owing to the spherical nature of the aggregates. Micelles with different sizes fuse up or get fragmented resulting in a change in the size of the micelles upon increasing the temperature keeping the water content constant. Construction of Voronoi area per head groups of BTMAC and SA superimposed with bilayer thickness and interdigitation for the bilayer indicates the presence of ripple phase at a lower temperature. As the temperature rises, the ripple phase of the bilayer transforms into an interdigitated gel phase ($L_{\beta I}$). Our simulations show that upon lowering the water content, the area per head-group (a_0) also decreases. The lowering in a_0 is coupled with an increment in the critical chain length (l_c) of the surfactants. An intricate balance between the coupled a_0 and l_c and the volume of the hydrophobic core lead to different packing parameters which is responsible for the aggregation of different macro-structures. Hence, our simulations unveil that the water concentration can play as an effectual variable in controlling the phases of amphiphilic molecules with desirable functionalities.

The work in this chapter is partly published in: Raju Lunkad, **Arpita Srivastava** and Ananya Debnath, Influence of water concentrations on the phase transformation of a model surfactant/co-surfactant/water system **2017**, Chemical Physics *483-484*, 103.